

RESEARCH ARTICLE | NOVEMBER 04 2022

Tip-scan high-speed atomic force microscopy with a uniaxial substrate stretching device for studying dynamics of biomolecules under mechanical stress

Feng-Yueh Chan ; Ryo Kurosaki; Christian Ganser ; Tetsuya Takeda; Takayuki Uchihashi  



Rev Sci Instrum 93, 113703 (2022)

<https://doi.org/10.1063/5.0111017>

 CHORUS



View
Online



Export
Citation

CrossMark

Tip-scan high-speed atomic force microscopy with a uniaxial substrate stretching device for studying dynamics of biomolecules under mechanical stress

Cite as: Rev. Sci. Instrum. 93, 113703 (2022); doi: 10.1063/5.0111017

Submitted: 18 July 2022 • Accepted: 9 October 2022 •

Published Online: 4 November 2022



View Online



Export Citation



CrossMark

Feng-Yueh Chan,¹  Ryo Kurosaki,¹ Christian Ganser,²  Tetsuya Takeda,³ and Takayuki Uchihashi^{1,2,4,a)} 

AFFILIATIONS

¹Department of Physics, Nagoya University, Chikusa-ku, Nagoya 464-8602, Japan

²Exploratory Research Center on Life and Living Systems (ExCELLS), National Institutes of Natural Sciences, 5-1 Higashiyama, Myodaiji, Okazaki, Aichi 444-8787, Japan

³Faculty of Medicine, Dentistry and Pharmaceutical Sciences, Okayama University, Kita-Ku, Okayama 700-8558, Japan

⁴Institute for Glyco-core Research (iGCORE), Nagoya University, Chikusa-ku, Nagoya 464-8602, Japan

^{a)}Author to whom correspondence should be addressed: uchihast@d.phys.nagoya-u.ac.jp

ABSTRACT

High-speed atomic force microscopy (HS-AFM) is a powerful tool for studying the dynamics of biomolecules *in vitro* because of its high temporal and spatial resolution. However, multi-functionalization, such as combination with complementary measurement methods, environment control, and large-scale mechanical manipulation of samples, is still a complex endeavor due to the inherent design and the compact sample scanning stage. Emerging tip-scan HS-AFM overcame this design hindrance and opened a door for additional functionalities. In this study, we designed a motor-driven stretching device to manipulate elastic substrates for HS-AFM imaging of biomolecules under controllable mechanical stimulation. To demonstrate the applicability of the substrate stretching device, we observed a microtubule buckling by straining the substrate and actin filaments linked by α -actinin on a curved surface. In addition, a BAR domain protein BIN1 that senses substrate curvature was observed while dynamically controlling the surface curvature. Our results clearly prove that large-scale mechanical manipulation can be coupled with nanometer-scale imaging to observe biophysical effects otherwise obscured.

Published under an exclusive license by AIP Publishing. <https://doi.org/10.1063/5.0111017>

I. INTRODUCTION

Atomic force microscopy (AFM)¹ has been widely adopted in various fields of academic research and industrial examinations for decades. While the development of AFM enabled observations of a wide variety of surfaces with resolution down to the atomic level, the imaging speed of several minutes per frame limited investigations to static samples. The emergence of high-speed AFM (HS-AFM) changed this paradigm by improving scanner design,^{2–4} system feedback bandwidth,^{5–7} and introducing miniaturized cantilevers.⁸ As a result, sub-second real-time imaging with the nanometer-scale resolution has been realized and allowed the observation of highly dynamic samples with single-molecule resolution.⁹ Combining the merits of low force perturbations¹⁰ and fast scanning, HS-AFM

became the go-to instrument not only for studying single-molecule dynamics but also for soft and delicate materials such as cells¹¹ and hydrogels.¹² In addition, the large number of images acquired by HS-AFM also enabled unprecedented high-resolution imaging of proteins by localization methods.¹³

The HS-AFM usually employs a compact and rigid sample scanner for X-, Y-, and Z-directions, keeping the cantilever stationary.¹⁴ While this setup leads to an improved system bandwidth compared to that of conventional AFMs, integration with a substrate manipulator or optical instruments is complex. Because the complications arise mainly due to the necessary small dimensions of the sample stage for rapid movement, a tip-scan type HS-AFM was developed.¹⁵ In contrast to the sample-scan HS-AFM, the tip-scan HS-AFM implements a piezo-actuated tip scanner and a

controllable dichroic mirror for tracking the cantilever-deflection-detection laser to the cantilever movement. Alternative to using an optics system for cantilever tracking, self-sensing cantilevers made of piezoresistive materials¹⁶ or tuning forks¹⁷ can convert the cantilever motion into electrical signals. However, the spring constant of the self-sensing cantilever is usually high for application to fragile biomolecules. Fixing the laser module with the probe module¹⁸ can eliminate the tracking problem, but also suffers the feedback bandwidth due to its increased size. As the tip-scanning configuration allows the sample stage to be stationary, it is possible to combine with other microscopic methods such as total internal reflection fluorescence microscopy¹⁵ and tip-enhanced optical imaging,¹⁹ and further would be expected to incorporate complex systems such as mechanical manipulation stage as described further in this work.

A major advantage of AFM over other microscopies is its functional flexibility. Not only surface topography but also conductivity, surface potential, and mechanical properties—among others—can be mapped on the nanometer scale. In particular, mechanical property measurements with AFM have gained attention and have become an indispensable tool in nano- and micromechanics.^{20,21} AFM-based nano- and micromanipulation techniques^{22,23} are part of the modern nanomechanical toolbox and provide an additional surface-focused perspective.^{24,25} While direct probing of surface mechanical properties with AFM is commonly used, it is also possible to apply large-scale deformations to the sample and monitor the changes in topography and surface mechanical properties. In a recent example of conventional AFM combined with large-scale substrate manipulation, Liu *et al.* reported polymer microdomain reorganization and localized changes in modulus.²⁶ To investigate the effect of the mechanical strain of elastomers in wearable devices, Cortelli *et al.* investigated the conductivity of the fracture gold layer on the elastomer substrate.²⁷ By combining localized conductivity measurements with large-scale strain, it was revealed that the tunneling effect permitted current to be transferred between fragments.²⁷ In the above-mentioned examples, conventional AFM was employed that limits the application to static or quasi-static effects. However, biological samples such as proteins are rarely static but highly dynamic. Such samples necessitate the use of HS-AFM when investigating the effects of mechanical deformation on their functions. In a recent example, bent microtubules were pinned on inhomogeneous lipid bilayers and observed by HS-AFM.²⁸ It was revealed that the walking speed of the motor protein kinesin is modulated by the microtubule curvature. However, the curvature of microtubules could not be changed in a well-controlled manner, limiting the accessible observation range to randomly found curvatures.

In this article, we report a uniaxial substrate stretching device combined with the tip-scan HS-AFM. Several devices combined with the AFM have been reported. De Jong *et al.* combined a compact stretching device with an AFM,²⁹ however, the strain is not precisely controlled by a stepper motor or other actuators. Hecht *et al.* designed a motor-driven bilateral stretching device for studying cell mechanics.³⁰ As no other flexure or actuator is there to displace the device, the sample needs to be incubated at the center, especially when subjected to a considerable strain, for sample tracking. The tracking will become more complicated if the stretching device unilaterally stretches the substrate.²⁴

Compared to the reported combined instruments, our stretching device is designed to have a compact size housed in a wide-range piezoelectric sample scanner with symmetrical and precise stretching motion. Thus, we can navigate to the region of interest and track it for molecule-level measurements without optical imaging. This device allows us to apply an arbitrary strain to an elastic substrate and, consequently, to samples adsorbed on its surface. As proof of functionality, we observed microtubule buckling and protein absorption on nanostructured surfaces with controllable curvature.

II. STRETCHING DEVICE

The tip-scan HS-AFM used in this study was built based on the previously reported model.¹⁵ The stretching device shown in Fig. 1(a), described in detail in Sec. II A, is hosted on an XY scanning stage that covers a wide range of $120 \times 120 \mu\text{m}^2$ (SFS-120XY, Sigmakoki, Japan) [Fig. 1(b)]. The tip-scan HS-AFM head is then placed on the XY scanning stage [Fig. 1(c)]. This means that in addition to high-speed scanning with the tip scanner, it is also possible to record wide-area images by scanning the stage, although at a lower speed (typically, 5 minutes per image). Manual micrometer heads are also used for coarse displacement of the XY fine stage.

A. Mechanical design

The stretching device shown in Fig. 1(a) consists of three major parts: a stepper motor with a power transmission mechanism, a pair of clips for holding the elastic substrate, and a support stage for the elastic substrate. A cross-sectional view of the model is shown in Fig. 1(d). A stepper motor actuates the device, and a screw mechanism converts the rotational motion into a linear displacement. The stepper motor is controlled by homemade software that sends digital pulses to the motor driver with an angular resolution of 0.036° per pulse. The linear displacement is converted via the aforementioned screw mechanism, with a thread pitch of 0.5 mm, to yield an overall displacement of 0.5 mm per 10000 pulses. This linear motion via the transmission shafts and the traction strings made by cotton yarn drives a pair of clips, which clamp the elastic substrate and move it along the gliding rails uniaxially and symmetrically. By applying even tension to the substrate from both sides and positioning the AFM tip near the center of the substrate, lateral movement of the observation area due to the stretching is suppressed, resulting in easier imaging of the same location. The stage was used to support the elastic substrate to laterally constrain the clips with a gliding structure during the movement. A thin layer of silicone oil was applied between the stage and the elastic substrate to reduce undesired friction. The detailed procedure for installing an elastic substrate to the stretching device can be found in the [supplementary material](#). The longitudinal strain applied to the substrate is estimated from the elongated length of the substrate divided by its initial length. For every 1000 pulses converted by the stepper motor into $50 \mu\text{m}$ linear displacement via the screw mechanism, both clips are driven $50 \mu\text{m}$ toward opposite directions from their original position. Consequently, the substrate length elongated from 10 to 10.1 mm, or 1% strain equivalently. The maximum strain to a 10 mm long substrate is 80%.

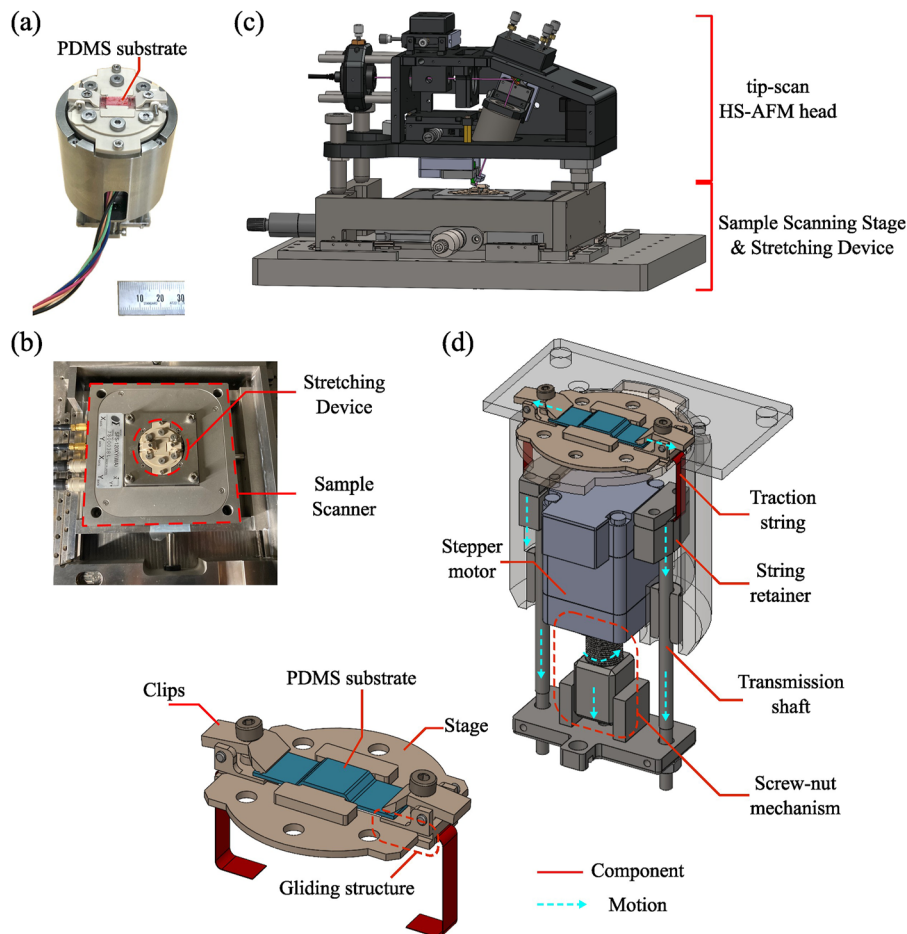


FIG. 1. Mechanical design of the substrate stretching device incorporated in a tip-scan HS-AFM. (a) An overhead view of the developed stretching device. A transparent polydimethylsiloxane (PDMS) substrate is colored with a red marker pen to improve visibility. (b) The stretching device is incorporated on the wide-field XY stage scanner, SFS-120(WA). (c) The compact tip-scan HS-AFM head is then placed above the presented stretching device. (d) A cross-section view of the rendering model of the assembled stretching device. A pair of clips that fixes the elastic substrate (drawn blue) is driven by the traction string (red). The stepper motor connected to the screw mechanism drives the traction string through the transmission rods and string retainer.

Although higher strain can be achieved by shortening the substrate length and related dimensions, the higher strain also leads to a pronounced surface wrinkle on the pristine elastic substrate,³¹ which is not favorable to AFM imaging. When we applied a strain of 1% to a 10 mm long substrate while imaging a region 2 mm away from the substrate's center along the stretching direction, we found that the imaging region was displaced by 20 μm . While it is desirable to take measurements at the center position of the substrate to restrain position shift due to stretching, it is impractical. As the center position relies on substrate geometry and relative position to the AFM probe, a feasible option for this issue is to limit the incremental strain of each stretching step and adjust the relative distance between the probe and the region of interest at each step. With a sufficient imaging scope and careful alignment with the micrometer heads and the wide-field XY scanner, it is possible to conduct observations of the same area at different strains without optical image assistance.

B. Strain characterization on a square-patterned elastic substrate

The strain in the nanometer- or micrometer-sized imaging area can be different from the globally applied strain to the sample.

Therefore, we directly measured the local strain and further quantified the Poisson effect by creating a regular square pattern on polydimethylsiloxane (PDMS) by molding the TGQ1 standard AFM calibration grating (NT-MDT, Russia). The TGQ1 grating was fixed by a drop of nail polish on the petri dish as a positive mold. The PDMS was prepared by mixing the two components of Sylgard 184 (Dow Corning, Japan) thoroughly at a 1:10 ratio. The resulting mixture was poured into the petri dish with the immobilized TGQ1 so that the grating was immersed completely. The mixture was then degassed in a vacuum desiccator for 30 min to eliminate bubbles. The PDMS was then cured in a 70 °C dry oven for 4 h and cooled down in the oven overnight. After cooling down, the PDMS was peeled from the TGQ1 surface. Finally, the PDMS was trimmed down to 5 × 14 mm² so that the TGQ1 pattern was located at the center. The substrate length between the clamps was 10 mm and was defined as the unstrained length.

The TGQ1 negative mold was clamped on the device and scanned at different longitudinal strains. The local strain was characterized by determining the pitch change of the periodic square pattern on the TGQ1 mold in the X and Y directions and the depth of the squares. The imaging was performed in pure water

at room temperature. The sample was stretched in 1 mm steps up to 7 mm (0%–70% global strain) at $10 \mu\text{m s}^{-1}$ and then reversed until the zero position was reached again. The cantilever used for the imaging was a BL-AC10DS-A2 (Olympus, Japan) with dimensions of $10 \mu\text{m}$ length, $2 \mu\text{m}$ width, and 130 nm thickness and a bird beak at the free end. The nominal spring constant of the cantilevers is 0.1 N/m . To prepare a sharp AFM probe, a carbon pillar was grown at the free end of the cantilever via electron beam deposition and then sharpened by plasma etching to obtain a radius at the tip apex of about 2 nm .³² All images were recorded in tapping mode. The cantilevers' resonance frequency was typically 510 kHz , the free amplitude was set to 4 nm , and the setpoint was 0.8 times the free amplitude.

The selected topographies recorded at different applied strains are shown in Fig. 2(a). The imaging areas were approximately maintained throughout the stretching and releasing. We can clearly see that the square patterns are elongated along the strain direction (vertical image direction; y) and conversely squeezed in transversal directions (horizontal image direction; x) as the stretching is increased. The original square pattern of TGQ1 has a periodicity of $3 \mu\text{m}$ in the X and Y directions and a height of 20 nm

according to the product specification. By the AFM images recorded with sample scan mode of the tip-scan HS-AFM, the negative mold of TGQ1 gave X and Y direction periodicity of $2.88 \pm 0.17 \mu\text{m}$ and $3.03 \pm 0.06 \mu\text{m}$ (mean \pm standard deviation, $N = 5$), respectively. The average depth of the patterns was $17.4 \pm 0.6 \text{ nm}$ ($N = 5$). Figure 2(b) shows the strains ϵ in the X , Y , and Z directions measured from the pattern dimensions as a function of the elongated length ΔL of the PDMS substrate. The strain ϵ in each direction is calculated by dividing the elongated or compressed length of the pattern dimensions by the respective initial values. The longitudinal strain ϵ_y under the elongated length of 7 mm was 0.73 , whereas the transversal strains ϵ_x and ϵ_z were 0.24 and 0.23 , respectively. After unstretching the substrate to its initial length, ϵ_x , ϵ_y , and ϵ_z were 1.5% , 1.9% , and 0.5% , respectively. These values are very low and fall within the error margin of the strain measurement. The ϵ_y vs elongated length ΔL can be fitted by a linear function with a regression coefficient of 0.998 , indicating that we can linearly stretch the elastic substrate along the longitudinal direction. Poisson's ratios for each direction ($\nu_{yx} = -\epsilon_x/\epsilon_y$, $\nu_{yz} = -\epsilon_z/\epsilon_y$) are plotted in Fig. 2(c). The Poisson's ratio of PDMS bulk material is typically between 0.4 – 0.5 .^{33–36} When a low amount of strain ($\epsilon_y = 0.1$) was applied,

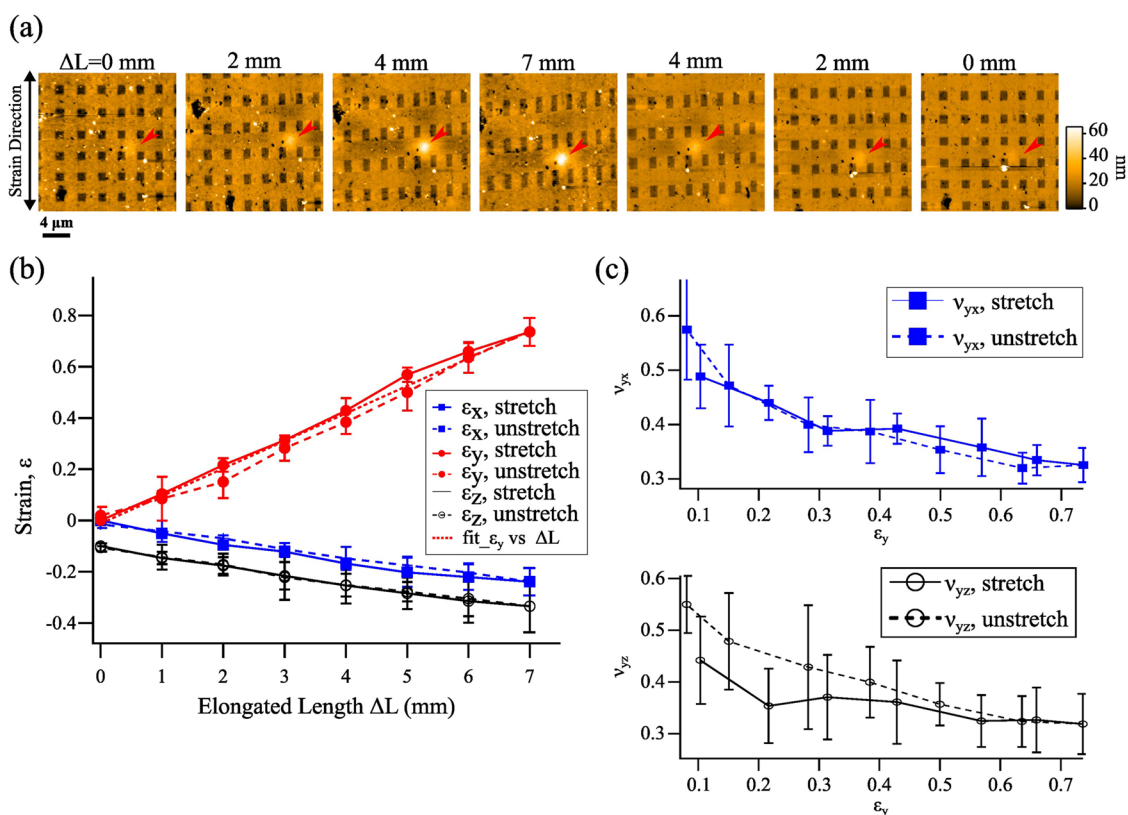


FIG. 2. Determination of the local strain during stretching a micropatterned PDMS substrate. (a) AFM images were taken with the stage scanner at successive 1 mm stretching steps (left to right). The nominal dimensions of the pattern were determined from the unstretched substrate. Stretching was stopped after the PDMS substrate was elongated by 7 mm. Sample-scan mode, $20 \times 20 \mu\text{m}^2$, 450×450 pixels. While releasing the strain from 7 mm extension back to 0 mm, AFM images were also recorded at the same intervals to confirm reversible deformation. (b) Strain vs substrate elongation in X -, Y -, and Z -directions. ϵ_z is shifted by -0.1 . (c) The Poisson's ratio ν_{yx} and ν_{yz} both decrease as longitudinal strain ϵ_y increases.

Poisson's ratios, $\nu_{yx} = 0.49$ and $\nu_{yz} = 0.44$, were found to be close to those of the bulk material. As the surface is textured by the regular square pattern, the Poisson's ratio decreased as ε_y increased and restored as ε_y decreased. The negative correlations between the longitudinal strain ε_y and Poisson's ratio ν_{yx} , ν_{yz} are consistent with previous observations of textured PDMS.³⁷ In Fig. 2(a), a cupola (indicated by a red arrow) can be seen developing during stretching, and it was fully reverted when the stress was released. This suggests that the cupola is related to the boundary disturbance exerted by clamping initially and propagated to the center area. Further investigation of the cupola with nanoindentation might provide deeper insight but is beyond the scope of this article. It is also obvious from Fig. 2(a) that the squares are gradually transforming into rhombi when the longitudinal strain exceeds 40%. However, the square shape was resumed when the strain was released to 30%. The pattern distortion is caused by the misalignment between the Y-axis of the TGQ1 pattern and the strain direction.

III. BIOIMAGING

With the proposed device, we can mechanically manipulate elastic substrates, such as PDMS or other copolymers, by stretching and releasing. At the same time, the characteristic change of the substrate or the incubated biomolecules can be investigated by tip-scan HS-AFM. Although PDMS is an ideal material for molding complex microchannels or other elaborate geometries, its surface's intrinsically hydrophobic nature hinders the formation of lipid bilayers³⁸ and induces protein denaturation.³⁹ To hydrophilize the PDMS surface, several treatments are available such as plasma etching,⁴⁰ UV-O₃ exposure,⁴¹ and acid treatment.⁴² These treatments basically oxidize the PDMS surface and create a hydrophilic silica-like layer that prevents nonspecific protein adsorption and improves lipid bilayer coverage. A side-effect of oxidation is that the surface becomes stiffer than the bulk material.⁴³ When applying compressive strain to such an oxidized surface, the mismatch in stiffness between bulk and surface will cause the surface to adopt a rippled conformation.⁴⁴ While the presented device can only apply tensile strain, the pronounced Poisson effect of PDMS results in significant compression normal to the direction of strain application. In that case, surface ripples will appear and orient parallel to the stretching axis.

While oxidation treatments are widely used to hydrophilize PDMS surfaces, the drastic changes in surface topography under stress may be undesirable depending on the application. In such cases, the surface may be used as is in conjunction with bovine serum albumin (BSA)⁴⁵ or casein⁴⁶ to hydrophilize the PDMS surface and prevent nonspecific adsorption. In addition, surfaces passivated by BSA or casein can be a base for attaching other proteins^{47,48} or further stack functional layers.⁴⁹ The protein or linkers will transfer the substrate's strain directly to the sample, allowing strain application to nanoscale samples via large-scale deformations while keeping the surface flat.

A. Controlled microtubule buckling under compressive load

Microtubules are the stiffest components in the cytoskeleton, making them an important target for understanding cell mechanics.

In particular, the buckling behavior of microtubules has attracted widespread attention.⁵⁰ Several methods have been verified for bending and buckling assays, including microtubules anchored by axonemes for optical tweezer⁵¹ and hydrodynamic deformation,⁵² biotin-streptavidin binding,⁵³ pinning by lipid defects,²⁸ and kinesin anchors on an elastic substrate.⁵⁴ Here, we employed the latter method, where kinesin was immobilized on an elastic substrate to anchor microtubules. The cargo-binding domain of kinesin is hydrophobic and can bind to hydrophobic PDMS surfaces without surface treatment due to hydrophobic interactions. Then, microtubules can be anchored with the microtubule-binding site of kinesin on the opposite side to the cargo-binding domain. We used recombinant kinesin-1 consisting of the first 573 amino acids.⁵⁵ Casein (C3400, Sigma-Aldrich) was mixed with the kinesin solution because casein can work as a blocking agent to prevent nonspecific binding of the kinesin-1 to the PDMS substrate. Microtubules were obtained by polymerizing tubulin purified from the porcine brain at 37 °C. To prevent the increase of dust due to agglomeration, the experiments were conducted on the same day the microtubules were polymerized.

First, kinesin solution was diluted to 100 nM by BRB80 buffer (80 mM PIPES, 1 mM EGTA, 1 mM MgCl₂, pH 6.8) containing 0.2 mg/ml casein. A pristine PDMS substrate (5 × 14 mm²) was fixed on the stage of the stretching device with a distance of 10 mm between the end of the clamps. The PDMS substrate was then elongated until the distance between the clamps was 15 mm. Then, the kinesin/casein solution was dropped on the preloaded PDMS surface to cover the PDMS surface with kinesin. After 20 min incubation, the sample was washed thoroughly by the BRB80/casein solution to remove residual kinesin-1 and casein molecules. Finally, the microtubule solution was incubated on the kinesin-covered PDMS surface for 30 minutes and rinsed with BRB80 containing 20 μM paclitaxel. The BRB80, including paclitaxel solution, was also used as the imaging buffer. An illustration of the microtubule buckling assay is shown in Fig. 3(a). The microtubules were compressed by releasing the preloaded PDMS substrate with a step of 0.25 mm, which is approximated to 1.65% strain, at a speed of 25 μm s⁻¹. The direction of strain application is parallel to the Y-axis of the AFM image. All images were acquired by sample-scan mode. Some topography features found on the PDMS surface on the images taken with 30 × 30 μm² at 400 pixels shown in Fig. 3(b) were used to navigate the sample stage and maintain the imaging scope. As can be seen in the images before and after the compression, the number of microtubules anchored on the PDMS substrate is reduced after the compression. This is likely because buckling of the microtubule decreases the anchor points with the substrate, resulting in detachment. In addition, mechanical stress by the compression may have induced microtubule depolymerization. We can also see that many of the microtubules remaining on the substrate after compression were ruptured. Figure 3(c) illustrates the bending of a single microtubule during the compression. The microtubule with a slight curve at the initial condition is bent even at 1.65% compression, and as the compressive strain is increased, the bending radius is clearly decreased. Figure 3(d) depicts the relation between bending radius and strains. At 3.3% strain, the bending radius was estimated to be 2000 nm by fitting a circle to the microtubule's shape. As expected, the bending radius decreased with increasing strain and was found to be 740 nm at 10% strain. When the strain reached

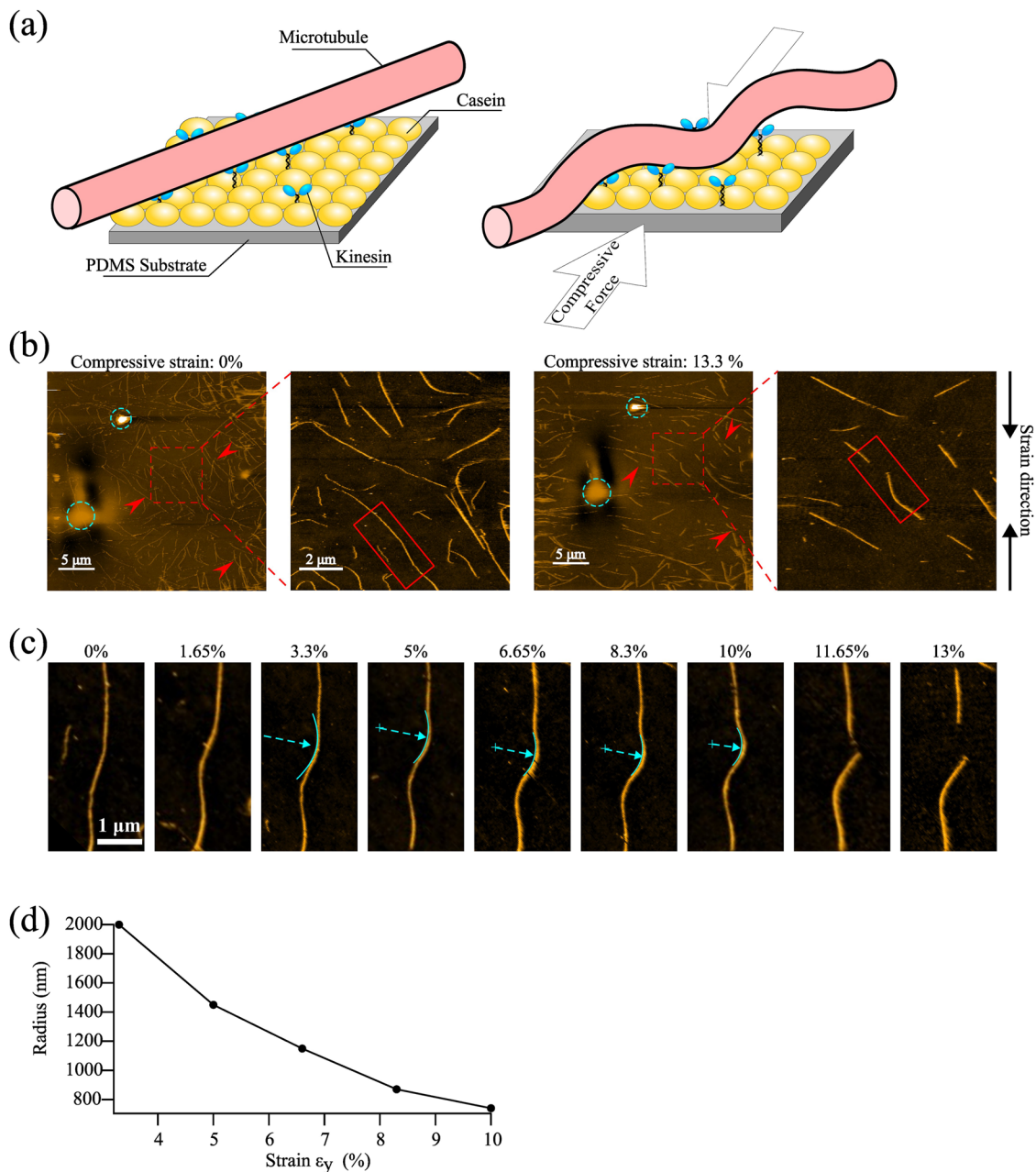


FIG. 3. Buckling of microtubules due to compression of PDMS substrate. (a) Illustration of the experimental setup. (b) Wide-area AFM images taken by the stage scanner before and after the substrate compression. Topography features encircled in cyan dashed circles were used to identify the identical microtubule throughout the experiment. Red arrows indicate other microtubules ruptured under compressive load. (c) Typical AFM images of the buckled microtubule recorded by sample stage scanning from 0%–13.3% compressive strain. (d) Bending radius along a microtubule as a function of applied strains.

11.7%, the bend radius became so small that the local deformations caused the microtubule to kink and break. At this point, the microtubule started to depolymerize partially, and the damage was found to have spread further at 13% strain.

The above microtubule buckling assay demonstrates the controllability of the curvature of microtubules with the stretching device. Furthermore, as the experiment was conducted on the HS-AFM, we anticipate studying the curvature-related mechanical

characteristics⁵⁶ as well as motor protein affinity by HS-AFM imaging with nanomechanics measurement.

B. Binding between actin filaments and α -actinin on a curved surface

Actin filament (F-actin) is also a part of the cytoskeleton, but unlike the rigid microtubules, F-actin is soft and flexible.⁵⁷ When a cell experiences external stress, the F-actins are reorganized, accompanied by the increased binding affinity of the cross-linker protein, α -actinin, during the process.⁵⁸ Here, we demonstrate an exemplary application of the stretching device to study the binding between α -actinin and actin filaments under strain.

To observe the cross-bridging of F-actins by α -actinin, F-actins must be moderately mobile while adsorbing to the substrate. Hence, F-actins were anchored onto the substrate via a lipid bilayer in this experiment. In order to form a lipid bilayer on a solid substrate, the surface must be hydrophilic. As mentioned above, hydrophilizing the PDMS surface hardens the surface, which enables us to create a ripple structure by applying mechanical strain.

The PDMS surface was hydrophilized by ion bombardment (PIB-10, Vacuum Device Inc., Japan) for 5 s. The PDMS substrate was then fixed on the stage and had an initial length of 10 mm between the clamps, and stretching was performed at $10 \mu\text{m s}^{-1}$. The PDMS surface with strain-dependent topography was imaged by sample-scan mode with $2 \times 2 \mu\text{m}^2$, 135×135 pixels, as shown in Fig. 4(a). Strains applied in the Y direction resulted in pronounced surface rippling in the transversal direction. The ripple structure had a certain angle with respect to the stretching direction. The angle increased as the applied strain increased. We believe this is caused by the substrate's longitudinal axis not being perfectly aligned with the stretching direction. This is the same reason why the square pattern transforms between square and rhombic shapes. A periodic pattern with the average peak-to-peak height H_{p-p} of 2 nm appeared only when the strain raised above 20%, as depicted in Fig. 4(b). The H_{p-p} below 20% strain was not discernible and increased as the strain increased. The wavelength of the ripples reached 402 nm at 35% strain and gradually decreased to 307 nm at 60% before slightly rising again to 356 nm at 70% [Fig. 4(c)]. On the other hand, the H_{p-p} of the ripples increased with strain, up to 67 nm at 70% strain applied.

To create a surface suitable for F-actin adsorption, a lipid bilayer with the following composition was prepared at a gravimetric ratio: 70% 1,2-dipalmitoyl-*sn*-glycero-3-phosphocholine (DPPC) (80355C, Avanti) and 30% 1,2-dipalmitoyl-3-trimethylammonium-propane (DPTAP) (890870, Avanti).⁵³ DPPC is charge neutral, while DPTAP is positively charged. Therefore, the adsorption affinity of negatively charged F-actin for lipid bilayers can be controlled to some extent by the DPTAP content.⁵⁹ $5 \mu\text{L}$ of DPPC/DPTAP lipid solution was incubated on the hydrophilized PDMS surface at 70°C for 20 min and then washed thoroughly with pure water. The substrate was mounted to the stretching device afterward. A solution of F-actins polymerized from G-actin (AKL99, Cytoskeleton, Inc.)⁶⁰ was incubated on the lipid bilayer-covered substrate for 10 min and flushed with the imaging buffer (20 mM Imidazole, 25 mM KCl, 2 mM MgCl_2 , 1 mM EGTA, and 1 mM DTT). As tip-scan HS-AFM images shown in Fig. 4(d), actin filaments were found abundantly on the lipid bilayer. After applying 30% strain

along the Y direction, surface buckling was induced, and the lipid bilayer together with the attached F-actins followed the topography.

To observe the strain dependence of α -actinin binding to F-actins, α -actinin was injected into the imaging buffer to a final concentration of 50 nM under different strain conditions. Figure 4(e) shows clipped images demonstrating α -actinin cross-bridging F-actins recorded by tip-scan HS-AFM with the imaging rate of 0.2 s/frame (Movie 1; Multimedia view, $\times 2$ playback). The HS-AFM images show that the α -actinin indicated by the arrow is stable during the imaging, while some are dynamically bound and dissociated. Figure 4(f) shows the typical HS-AFM images of α -actinin bound to F-actins on the flat substrate and a rippled substrate under 40% strain. We found that α -actinins bound to F-actins adsorbed on the curved substrate, i.e., F-actins under mechanical stress due to bending, in a much denser and more ordered fashion than on the unstrained substrate. The average distances between adjacent α -actinins for the flat and curved substrates were 14.5 and 9.0 nm, respectively, as estimated from the HS-AFM images shown in Fig. 4(f). Detail about the estimation can be found in Fig. S1. Previous studies have suggested that the binding affinity of α -actinin to F-actin under tension is enhanced,⁵⁶ consistent with our initial results. Although the detailed molecular mechanisms underlying the phenomena observed here require further investigation, the combination of the stretching device and HS-AFM has been demonstrated to be useful in studying the mechanosensitive dynamics of actin-binding proteins to F-actin.

C. Membrane curvature sensing of BIN1

Bridging Integrator-1 (BIN1) is a protein also known as myc box-dependent interacting protein 1 and amphiphysin-2. BIN1 can sense the curvature of the lipid⁶¹ and participates in endocytosis and membrane trafficking. Several diseases are related to the anomalous behavior of BIN1, such as centronuclear myopathy (CNM)⁶² and Alzheimer's disease.⁶³ We here observed curvature-dependent binding dynamics of BIN1 by tip-scan HS-AFM on a lipid bilayer surface with controllable curvature created using a stretching device.

Although oxidization treatment yields a hydrophilic layer on the PDMS surface, as described above, the negatively charged surface was unsuitable for creating a homogeneous layer of negatively charged lipids needed for interaction with BIN1. To improve the vesicle adhesion and fusion on the surface, we treated the oxidized PDMS with (3-aminopropyl) triethoxysilane (APTES) to create a positively charged surface suitable for negatively charged lipid bilayer formation.⁶⁴ The detailed procedure to create the substrates is as follows: A new PDMS substrate was covered by masking tape with an opening of 4.5 mm diameter and transferred into the UV ozone cleaner (Ossila, UK) and treated for 1 h. After the UV- O_3 treatment, the surface not covered by the mask was immediately immersed in 0.1% APTES for 1 min and thoroughly flushed with pure water. To observe the binding of BIN1, the following lipid mixture was prepared according to literature⁶⁵ at a gravimetric ratio: 64% PS (840032C, Avanti), 2% PI(4,5) P_2 (805155P, Avanti), 14% PE (840022C, Avanti), and 20% Cholesterol (70000P, Avanti). The lipid solution was then diluted by a

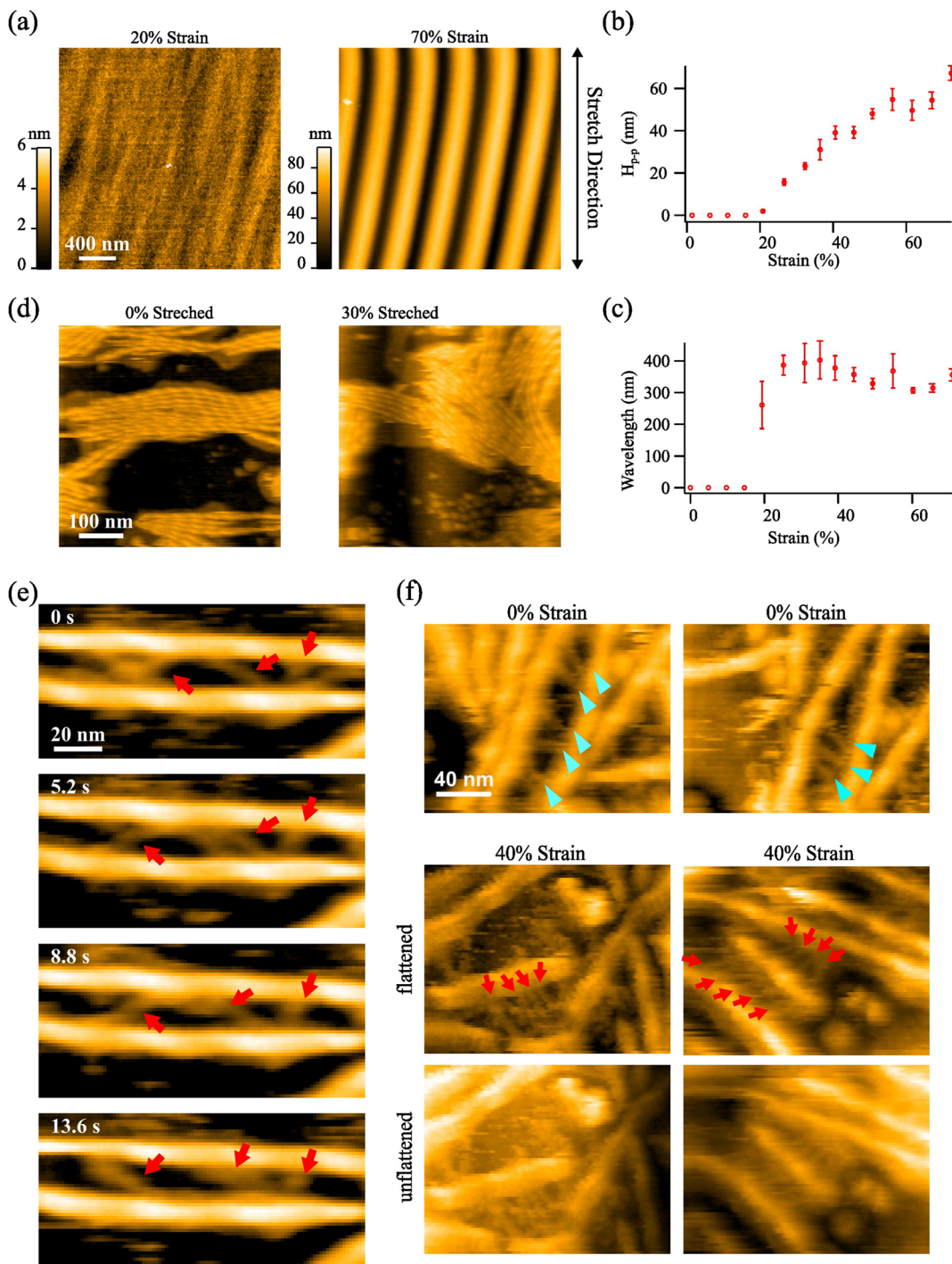


FIG. 4. Actin filaments crosslinked by α -actinin on locally curved PDMS surfaces created by ion bombardment. (a) The geometry of the surface ripples can be controlled by applying the strain to the PDMS substrate. (b) The peak-to-peak height, H_{p-p} , and (c) wavelength of rippled surfaces were measured as a function of applied substrate strains. (d) Deposited actin filaments conformed to the local surface curvature, making it possible to control actin bending. Tip-scan mode, $500 \times 500 \text{ nm}^2$ at 150 pixels per direction at 1 second per frame. (e) HS-AFM image of binding between α -actinin and actin-filaments taken with the tip-scan mode. Scan area, $135 \times 64 \text{ nm}^2$ at 101×48 pixels. Imaging rate, 200 ms/frame. (See Movie 1; Multimedia view, $\times 2$ playback). (f) α -actinin binding at 0% strain (pointed by cyan triangles) and at 40% strain (pointed by red arrows). Imaging mode, tip-scan mode. Scan area, $180 \times 140 \text{ nm}^2$ at 136×73 pixels. Imaging rate, 200 ms/frame. Multimedia view: <https://doi.org/10.1063/5.0111017.1>.

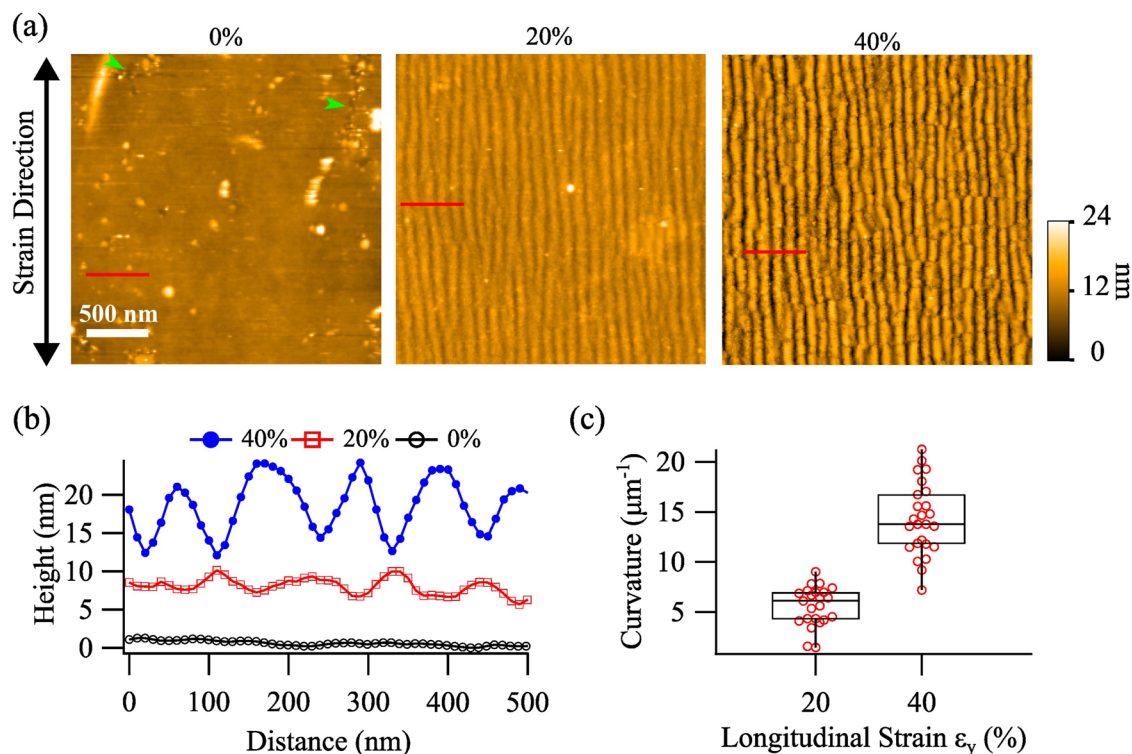


FIG. 5. Strain-dependent topography of a supported lipid bilayer on the UV- O_3 /APTES treated PDMS substrate. (a) AFM images of the surface at strain values of 0%, 20%, and 40%. Imaging mode, sample scan. Scan area, $2.5 \times 2.5 \mu\text{m}^2$ at 250×250 pixels. The green arrows shown in (a) indicate cracks on the lipid bilayer. (b) Exemplary line profiles normal to the ripples are indicated by red lines in (a). The profiles are shifted by 5 and 10 nm for 20% and 40% strain, respectively. (c) Curvatures of the ripple apex are determined from line profiles. See the text for details of curvature calculation.

tris-based buffer to a concentration of 0.1 mg/ml and sonicated for 15 s by a tip sonicator (NR-50M, Microtec Co. Ltd., Japan) before usage. 5 μL of the lipid mixture containing PI(4,5)P₂ was incubated on the silanized PDMS surface at 55 °C for 20 min and washed thoroughly first with pure water and then with cytosolic buffer (25 mM HEPES, 25 mM KCl, 2.5 mM Magnesium acetate, 0.1 M K-glutamate, pH 7.2). Figure 5(a) shows the lipid bilayer almost entirely covering the PDMS surface except for partial cracks, as indicated by arrows. Recombinant BIN1 K436X, which is a mutant with enhanced membrane deformation capacity,⁶³ was diluted by the cytosolic buffer to 2.1 μM and injected into the AFM observation buffer (same as the cytosolic buffer) to a final concentration of 25 nM. The dynamics of BIN1 binding/dissociation were observed by tip-scan HS-AFM by stretching the PDMS substrate to a length of 12 mm (20% strain) and 14 mm (40% strain) from an initial distance of 10 nm.

Applying stress along the Y direction, surface rippling along the X direction was developed on the lipid-covering PDMS surface [Fig. 5(a)]. The curvature of the surface was determined by solving the equation of a circle with three points given on a line profile of a ripple, including the apex and two neighboring points 20 nm away (see Fig. S2). As demonstrated in Sec. III B, the curvature of the lipid bilayer is controllable, as is evident from Figs. 5(b) and 5(c). The average ripple curvature at 20% and 40% tensile strain applied

was 5.59 and 14.27 μm^{-1} , respectively. Interestingly, the ripple structure induced on the PDMS surface with the UV- O_3 treatment is smaller than that of the PDMS surface after the ion bombardment described above, i.e., the amplitudes of the ripple structure of the PDMS at 40% strain were about 40 and 10 nm after the ion bombardment and the UV- O_3 treatment, respectively. This is because the hard layer formed on the PDMS surface by the ion-bombardment hydrophilization is thicker than by UV- O_3 treatment,⁶⁶ indicating that the amplitude of the ripple structure can be controlled by both the method of hydrophilization and strain application. In addition, the gentler ripple structure by UV- O_3 treatment enabled producing the large curvatures.

First, we attempted to observe the binding of BIN1 to the flat lipid without stretching but were unable to confirm any apparent binding [Fig. 6(a)]. This indicates that the interaction of BIN1 with the flat lipid, even in affinity-enhancing CNM-associated mutant K436X, is weak enough to be easily detached by disturbance from the AFM tip, or the binding time is at least much shorter than the time resolution of HS-AFM where we used the fastest imaging rate of 0.1 s/frame. On the other hand, BIN1 binding was clearly observed on lipid membrane surfaces with curvature even at imaging speeds of 0.5 s/frame [Fig. 6(a)] (also see Movies 2 and 3; Multimedia view, $\times 2$ playback). As an example of the interaction of BIN1 with a curved lipid surface, the clipped HS-AFM

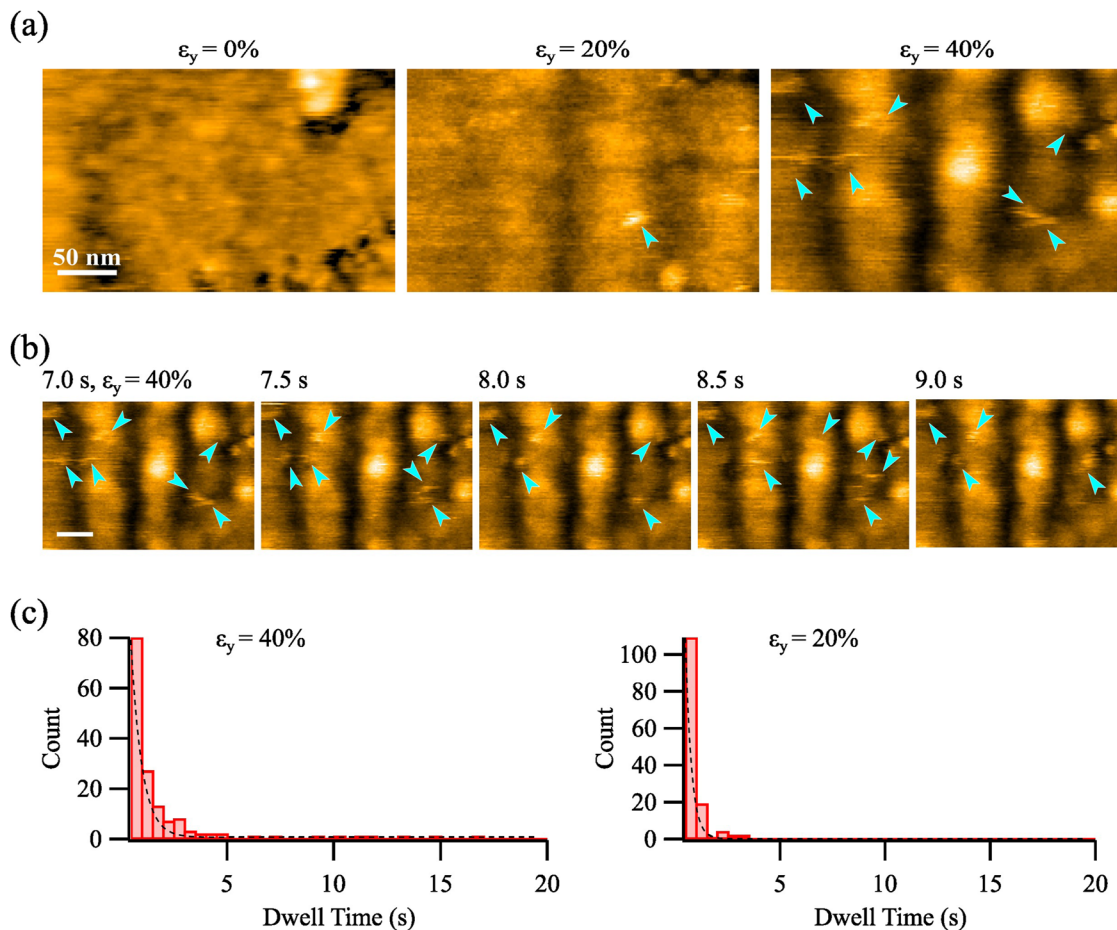


FIG. 6. Curvature-dependent binding of BIN1 K436X. (a) BIN1 bound to a surface under 40% strain with high local curvature, 20% strain with low local curvature, and a flat surface. Imaging mode, tip scan. Scan area, $300 \times 210 \text{ nm}^2$ at 150×105 pixels. Imaging rate, 500 ms/frame. (b) Snapshots of the dynamic binding and dissociation process of BIN1 to the highly curved surface at 40% strain. Imaging mode, tip scan. Scan area, $300 \times 210 \text{ nm}^2$ at 150×105 pixels. Imaging rate, 500 ms/frame. (See Movies 2 and 3; Multimedia view, $\times 2$ playback). (c) Within the same time, the dwell time of BIN1 was higher at the 40% strained surface compared to the 20% strained surface (103 frames, $N_{40\%} = 153$, $N_{20\%} = 137$). Multimedia views: <https://doi.org/10.1063/5.0111017.2>; <https://doi.org/10.1063/5.0111017.3>.

images captured on the substrate under 40% strain application are shown in Fig. 6(b). Most BIN1 molecules were stably bound near the top of a lipid-covered ripple and less so at the sides and the bottom, suggesting preferential binding to the positive curvature region. In addition, the average numbers of BIN1 proteins bound to the lipid surface per frame were 5.8 ± 1.7 and 1.8 ± 1.1 ($N = 103$ frames) at 40% and 20% strain, counted within a scanning area of $300 \times 210 \text{ nm}^2$, respectively, confirming that BIN1 has a higher affinity to surfaces with a larger curvature.^{61,67} The dwell time analysis of BIN1 on the curved surfaces is shown in Fig. 6(c). The histograms of dwell time were fitted with the single exponential decay function, giving the time constant τ for 20% and 40% strain surface of $1.83 \pm 0.09 \text{ s}$ and $3.77 \pm 0.06 \text{ s}$, respectively. This indicates that the difference in lipid curvature between $5.59 \mu\text{m}^{-1}$ (20% strain) and $14.27 \mu\text{m}^{-1}$ (40% strain) induces an almost two-fold difference in the affinity. In previous studies, the interaction between BIN1 and lipids could only be analyzed as a change in fluorescence

intensity due to the binding of BIN1 to different curvatures of the lipid.^{61,67} In contrast, our system can directly measure the dynamics of binding and dissociation depending on the lipid curvature at the single-molecule level.

IV. CONCLUSION

In this article, we described an instrument that combines the capability of uniaxially stretching elastomer substrates with simultaneous HS-AFM for studying nanometer-scale dynamics of biological samples under mechanical stress. The uniaxial stretching system developed can stretch an elastomeric substrate to approximately twice its initial length with an accuracy of 50 nm per step. The tip-scan HS-AFM allowed space around the sample and facilitated the incorporation of the stretching device into the AFM stage. Furthermore, using a scanner that covers a $120 \times 120 \mu\text{m}^2$ range enabled wide-area, low-speed AFM imaging and relatively easy

compensation of positional changes caused substrate stretching. We evaluated the performance of the stretching device using square patterns molded in PDMS. It was possible to take AFM images of the square patterns at the same location while applying strain and confirmed that the square pattern stretches linearly in the longitudinal direction and simultaneously shrinks in the transverse direction due to Poisson's effect.

The applicability of HS-AFM with an incorporated stretching system to biophysical problems was demonstrated by three challenging experiments. First, in a microtubule bending experiment, a compressive load was cumulatively applied via kinesin anchors bound to the elastic substrate. Then, we succeeded in inducing buckling and further fracture of microtubules by applying strain to the substrate. In the second demonstration, the binding of α -actinin to F-actin was investigated on a highly rippled surface created by a combination of ion bombardment of PDMS and the stretching device, with results suggesting that the strain may increase the density of α -actinin cross-bridging F-actin due to the bending.

Finally, by creating PDMS surfaces with gentle ripples by UV-O₃ treatment, we succeeded in observing the membrane curvature-dependent binding affinity of BIN1. As a result, BIN1 binding to flat lipid membranes was not observed, indicating that the binding affinity of the flat membrane is too weak to be detected by our HS-AFM. In contrast, BIN1 is repeatedly bound to and dissociated from the curved membrane. The curvature-sensitive adsorption of the BIN1 mutant K436X was confirmed with high-speed scanning. Furthermore, the dwell time analysis of BIN1 on the curved membrane showed a two-fold higher affinity to the membrane with a curvature of $5.59 \mu\text{m}^{-1}$ to that of $14.27 \mu\text{m}^{-1}$.

With these three examples, we demonstrated that the combination of substrate stretching with HS-AFM is a powerful tool for nano- and micromechanical investigations of biological samples. To further extend the functionality, substrate stretching can be coupled with nanomechanical measurements such as in-line force-curve measurements.⁶⁸ This would not only give insights into the strain-dependent mechanical properties of biopolymers, such as microtubules, but could also be applied to study how cells react to external stimuli. Moreover, the applications are not only limited to biophysical problems and could easily encompass materials science of soft matter, where often time-dependent material properties, such as viscoelasticity, are encountered.

SUPPLEMENTARY MATERIAL

Estimation of the average distance of adjacent α -actinins was described in the text with Fig. S1. Curvature estimation of the rippled structure was described in the text with Fig. S2. Determination procedure of the clamp position at an elastic substrate was described at the end of the [supplementary material](#).

ACKNOWLEDGMENTS

This work was supported by Kakenhi Grant No. 20K03889 to C.G., Grant Nos. 21H01772 and 21H00393 to T.U., and Grant No. 19KK0180 to T.T. and T.U. and by JST, CREST Grant No. JPMJCR21L2, Japan. The authors thank Professor Akira Kakugo

and Dr. Syeda Rubaiya Nasrin at Hokkaido University for providing kinesin-1 and Professor Takuya Sasaki and Dr. Ayuko Sakane at Tokushima University for providing α -actinin.

AUTHOR DECLARATIONS

Conflict of Interest

The authors have no conflicts to disclose.

Author Contributions

Feng-Yueh Chan: Conceptualization (equal); Formal analysis (lead); Investigation (lead); Methodology (lead); Software (equal); Writing – original draft (lead). **Ryo Kurosaki:** Formal analysis (equal); Investigation (equal); Methodology (supporting). **Christian Ganser:** Funding acquisition (equal); Investigation (equal); Methodology (supporting); Software (equal); Writing – review & editing (equal). **Tetsuya Takeda:** Funding acquisition (equal); Investigation (equal); Writing – review & editing (supporting). **Takayuki Uchihashi:** Conceptualization (lead); Funding acquisition (lead); Project administration (lead); Software (lead); Supervision (lead).

DATA AVAILABILITY

The data that support the findings of this study are available from the corresponding author upon reasonable request.

REFERENCES

- 1 G. Binnig, C. F. Quate, and C. Gerber, *Phys. Rev. Lett.* **56**, 930 (1986).
- 2 T. Ando, N. Kodera, E. Takai, D. Maruyama, K. Saito, and A. Toda, *Proc. Natl. Acad. Sci. U. S. A.* **98**, 12468 (2001).
- 3 T. Sulchek, R. Hsieh, J. D. Adams, G. G. Yaralioglu, S. C. Minne, and C. F. Quate, *Appl. Phys. Lett.* **76**, 1473 (2000).
- 4 L. M. Picco, L. Bozec, A. Ulcinas, D. J. Engledew, M. Antognozzi, M. A. Horton, and M. J. Miles, *Nanotechnology* **18**, 044030 (2007).
- 5 G. Schitter, K. J. Astrom, B. E. DeMartini, P. J. Thurner, K. L. Turner, and P. K. Hansma, *IEEE Trans. Control Syst. Technol.* **15**, 906 (2007).
- 6 B. J. Kenton, A. J. Fleming, and K. K. Leang, *Rev. Sci. Instrum.* **82**, 123703 (2011).
- 7 N. Kodera, M. Sakashita, and T. Ando, *Rev. Sci. Instrum.* **77**, 083704 (2006).
- 8 M. Kitazawa, K. Shiotani, and A. Toda, *Jpn. J. Appl. Phys.* **42**, 4844 (2003).
- 9 T. Ando, T. Uchihashi, and S. Scheuring, *Chem. Rev.* **114**, 3120 (2014).
- 10 A. P. Nievergelt, N. Banterle, S. H. Andany, P. Gönczy, and G. E. Fantner, *Nat. Nanotechnol.* **13**, 696 (2018).
- 11 M. Shibata, T. Uchihashi, T. Ando, and R. Yasuda, *Sci. Rep.* **5**, 8724 (2015).
- 12 Y. Nishizawa, H. Minato, T. Inui, T. Uchihashi, and D. Suzuki, *Langmuir* **37**, 151 (2021).
- 13 G. R. Heath, E. Kots, J. L. Robertson, S. Lansky, G. Khelashvili, H. Weinstein, and S. Scheuring, *Nature* **594**, 385 (2021).
- 14 T. Ando, T. Uchihashi, and T. Fukuma, *Prog. Surf. Sci.* **83**, 337 (2008).
- 15 M. Mahdavi, M. B. Coskun, and S. O. R. Moheimani, *J. Microelectromech. Syst.* **29**, 260 (2020).
- 16 T. Akiyama, U. Stauffer, and N. F. de Rooij, *Appl. Surf. Sci.* **210**, 18 (2003).
- 17 M. Balantekin, S. Satir, D. Torello, and F. L. Değertekin, *Rev. Sci. Instrum.* **85**, 123705 (2014).
- 18 S. Fukuda, T. Uchihashi, R. Iino, Y. Okazaki, M. Yoshida, K. Igarashi, and T. Ando, *Rev. Sci. Instrum.* **84**, 073706 (2013).
- 19 T. Umakoshi, S. Fukuda, R. Iino, T. Uchihashi, and T. Ando, *Biochim. Biophys. Acta, Gen. Subj.* **1864**, 129325 (2020).

- ²⁰M. Rief, M. Gautel, F. Oesterhelt, J. M. Fernandez, and H. E. Gaub, *Science* **276**, 5315 (1997).
- ²¹R. Garcia, *Chem. Soc. Rev.* **49**, 5850 (2020).
- ²²B. R. Neugirg, S. R. Koebly, H. C. Schniepp, and A. Fery, *Nanoscale* **8**, 8414 (2016).
- ²³S. R. Baker, S. Banerjee, K. Bonin, and M. Guthold, *Mater. Sci. Eng. C* **59**, 203 (2016).
- ²⁴D. Ahrens, W. Rubner, R. Springer, N. Hampe, J. Gehlen, T. M. Magin, B. Hoffmann, and R. Merkel, *Methods Protoc.* **2**, 43 (2019).
- ²⁵G. Tagiltsev, C. A. Haselwandter, and S. Scheuring, *Sci. Adv.* **7**, eabg9934 (2021).
- ²⁶H. Liu, X. Liang, and K. Nakajima, *Jpn. J. Appl. Phys.* **59**, SN1013 (2020).
- ²⁷G. Cortelli, L. Patrino, T. Cramer, B. Fraboni, and S. de Miranda, *ACS Appl. Electron. Mater.* **4**, 2831 (2022).
- ²⁸S. R. Nasrin, C. Ganser, S. Nishikawa, A. R. Kabir, K. Sada, T. Yamashita, M. Ikeguchi, T. Uchihashi, H. Hess, and A. Kakugo, *Sci. Adv.* **7**, eabf2211 (2021).
- ²⁹K. L. De Jong, H. C. MacLeod, P. R. Norton, N. O. Petersen, and M. F. Jasnin, *Rev. Sci. Instrum.* **77**, 023701 (2006).
- ³⁰E. Hecht, P. Knittel, E. Felder, P. Dietl, B. Mizaikoff, and C. Kranz, *Analyst* **137**, 5208 (2012).
- ³¹E. Puntel, L. Deseri, and E. Fried, *J. Elasticity* **105**, 137 (2011).
- ³²T. Uchihashi, N. Kodera, and T. Ando, *Nat. Protoc.* **7**, 1193 (2012).
- ³³A. T. Sepúlveda, R. G. de Villoria, J. C. Viana, A. J. Pontes, B. L. Wardle, and L. A. Rocha, *Nanoscale* **5**, 4847 (2013).
- ³⁴S. Dogru, B. Aksoy, H. Bayraktar, and B. E. Alaca, *Polym. Test.* **69**, 375 (2018).
- ³⁵A. Müller, M. C. Wapler, and U. Wallrabe, *Soft Matter* **15**, 779 (2019).
- ³⁶I. D. Johnston, D. K. McCluskey, C. K. L. Tan, and M. C. Tracey, *J. Micromech. Microeng.* **24**, 035017 (2014).
- ³⁷H. Liu, J. Yan, M. Kollasche, S. A. Bentil, and S. Laflamme, *Smart Mater. Struct.* **29**, 105037 (2020).
- ³⁸P. Lenz, C. M. Ajo-Franklin, and S. G. Boxer, *Langmuir* **20**, 11092 (2004).
- ³⁹A. G. Richter and I. Kuzmenko, *Langmuir* **29**, 5167 (2013).
- ⁴⁰S. L. Peterson, A. McDonald, P. L. Gourley, and D. Y. Sasaki, *J. Biomed. Mater. Res. A* **72A**, 10 (2005).
- ⁴¹Y. Berdichevsky, J. Khandurina, A. Guttman, and Y.-H. Lo, *Sens. Actuators, B* **97**, 402 (2004).
- ⁴²D. Maji, S. K. Lahiri, and S. Das, *Surf. Interface Anal.* **44**, 62 (2012).
- ⁴³K. L. Mills, X. Zhu, S. Takayama, and M. D. Thouless, *J. Mater. Res.* **23**, 37 (2008).
- ⁴⁴N. Bowden, W. T. S. Huck, K. E. Paul, and G. M. Whitesides, *Appl. Phys. Lett.* **75**, 2557 (1999).
- ⁴⁵W. Roos, J. Ulmer, S. Gräter, T. Surrey, and J. P. Spatz, *Nano Lett.* **5**, 2630 (2005).
- ⁴⁶W. H. Roos, O. Campàs, F. Montel, G. Woehlke, J. P. Spatz, P. Bassereau, and G. Cappello, *Phys. Biol.* **5**, 046004 (2008).
- ⁴⁷T. Ozeki, V. Verma, M. Uppalapati, Y. Suzuki, M. Nakamura, J. M. Catchmark, and W. O. Hancock, *Biophys. J.* **96**, 3305 (2009).
- ⁴⁸V. Verma, W. O. Hancock, and J. M. Catchmark, *J. Biol. Eng.* **2**, 14 (2008).
- ⁴⁹Y. Jeong, K. Choi, J. Kim, D. S. Chung, B. Kim, H. C. Kim, and K. Chun, *Sens. Actuators, B* **128**, 349 (2008).
- ⁵⁰T. Li, *J. Biomech.* **41**, 1722 (2008).
- ⁵¹H. Felgner, R. Frank, and M. Schliwa, *J. Cell Sci.* **109**, 509 (1996).
- ⁵²P. Venier, A. C. Maggs, M. F. Carlier, and D. Pantaloni, *J. Biol. Chem.* **269**, 13353 (1994).
- ⁵³H. Hess, J. Howard, and V. Vogel, *Nano Lett.* **2**, 1113 (2002).
- ⁵⁴D. Inoue, B. Mahmot, A. M. R. Kabir, T. I. Farhana, K. Tokuraku, K. Sada, A. Konagaya, and A. Kakugo, *Nanoscale* **7**, 18054 (2015).
- ⁵⁵K. Fujimoto, M. Kitamura, M. Yokokawa, I. Kanno, H. Kotera, and R. Yokokawa, *ACS Nano* **7**, 447 (2013).
- ⁵⁶E. Memet, F. Hilitiski, M. A. Morris, W. J. Schwenger, Z. Dogic, and L. Mahadevan, *Elife* **7**, e34695 (2018).
- ⁵⁷J. Stricker, T. Falzone, and M. L. Gardel, *J. Biomech.* **43**, 9 (2010).
- ⁵⁸T. Luo, K. Mohan, P. A. Iglesias, and D. N. Robinson, *Nat. Mater.* **12**, 1064 (2013).
- ⁵⁹D. Yamamoto, T. Uchihashi, N. Kodera, H. Yamashita, S. Nishikori, T. Ogura, M. Shibata, and T. Ando, *Methods Enzymol.* **475**, 541 (2010).
- ⁶⁰X. Zhang, X. Hu, H. Lei, J. Hu, and Y. Zhang, *Nanoscale* **8**, 6008 (2016).
- ⁶¹M. B. Jensen, V. K. Bhatia, C. C. Jao, J. E. Rasmussen, S. L. Pedersen, K. J. Jensen, R. Langen, and D. Stamou, *J. Biol. Chem.* **286**, 42603 (2011).
- ⁶²K. Fujise, S. Noguchi, and T. Takeda, *Int. J. Mol. Sci.* **23**, 6274 (2022).
- ⁶³P. L. De Jager, G. Srivastava, K. Lunnon, J. Burgess, L. C. Schalkwyk, L. Yu, M. L. Eaton, B. T. Keenan, J. Ernst, C. McCabe, A. Tang, T. Raj, J. Replogle, W. Brodeur, S. Gabriel, H. S. Chai, C. Younkin, S. G. Younkin, F. Zou, M. Szyf, C. B. Epstein, J. A. Schneider, B. E. Bernstein, A. Meissner, N. Ertekin-Taner, L. B. Chibnik, M. Kellis, J. Mill, and D. A. Bennett, *Nat. Neurosci.* **17**, 1156 (2014).
- ⁶⁴P. Taylor, C. Xu, P. D. I. Fletcher, and V. N. Paunov, *Phys. Chem. Chem. Phys.* **5**, 4918 (2003).
- ⁶⁵K. Fujise, M. Okubo, T. Abe, H. Yamada, I. Nishino, S. Noguchi, K. Takei, and T. Takeda, *J. Biol. Chem.* **296**, 100077 (2021).
- ⁶⁶F. A. Bayley, J. L. Liao, P. N. Stavrinou, A. Chiche, and J. T. Cabral, *Soft Matter* **10**, 1155 (2014).
- ⁶⁷L.-L. Li, Q.-J. Guo, H.-Y. Lou, J.-H. Liang, Y. Yang, X. Xing, H.-T. Li, J. Han, S. Shen, H. Li, H. Ye, H. Di Wu, B. Cui, and S.-Q. Wang, *Nano Lett.* **20**, 6387 (2020).
- ⁶⁸C. Ganser and T. Uchihashi, *Nanoscale* **11**, 125 (2019).